

A combined helium atom scattering and density-functional theory study of the Nb(100) surface oxide reconstruction: Phonon band structures and vibrational dynamics

Cite as: J. Chem. Phys. 156, 124702 (2022); <https://doi.org/10.1063/5.0085653>

Submitted: 18 January 2022 • Accepted: 02 March 2022 • Published Online: 22 March 2022

 Alison A. McMillan, Caleb J. Thompson,  Michelle M. Kelley, et al.



View Online



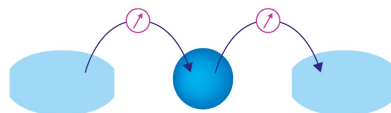
Export Citation



CrossMark

Webinar

Interfaces: how they make
or break a nanodevice



March 29th – Register now



Zurich
Instruments

AIP
Publishing

A combined helium atom scattering and density-functional theory study of the Nb(100) surface oxide reconstruction: Phonon band structures and vibrational dynamics

Cite as: J. Chem. Phys. 156, 124702 (2022); doi: 10.1063/5.0085653

Submitted: 18 January 2022 • Accepted: 2 March 2022 •

Published Online: 22 March 2022








View Online



Export Citation



CrossMark

Alison A. McMillan,¹  Caleb J. Thompson,¹ Michelle M. Kelley,²  Jacob D. Graham,¹  Tomás A. Arias,² 
and S. J. Sibener^{1,a)} 

AFFILIATIONS

¹Department of Chemistry and The James Franck Institute, The University of Chicago, 929 E. 57th Street, Chicago, Illinois 60637, USA

²Department of Physics, Cornell University, Ithaca, New York 14853, USA

^{a)}Author to whom correspondence should be addressed: s-sibener@uchicago.edu

ABSTRACT

Helium atom scattering and density-functional theory (DFT) are used to characterize the phonon band structure of the (3×1) -O surface reconstruction of Nb(100). Innovative DFT calculations comparing surface phonons of bare Nb(100) to those of the oxide surface show increased resonances for the oxide, especially at higher energies. Calculated dispersion curves align well with experimental results and yield atomic displacements to characterize polarizations. Inelastic helium time-of-flight measurements show phonons with mixed longitudinal and shear-vertical displacements along both the $\langle 100 \rangle$, $\overline{1}X$ and $\langle 110 \rangle$, $\overline{1}M$ symmetry axes over the entire first surface Brillouin zone. Force constants calculated for bulk Nb, Nb(100), and the (3×1) -O Nb(100) reconstruction indicate much stronger responses from the oxide surface, particularly for the top few layers of niobium and oxygen atoms. Many of the strengthened bonds at the surface create the characteristic ladder structure, which passivates and stabilizes the surface. These results represent, to our knowledge, the first phonon dispersion data for the oxide surface and the first *ab initio* calculation of the oxide's surface phonons. This study supplies critical information for the further development of advanced materials for superconducting radiofrequency cavities.

Published under an exclusive license by AIP Publishing. <https://doi.org/10.1063/5.0085653>

I. INTRODUCTION

Particle accelerators are used in a wide range of disciplines, including high-energy particle physics, chemistry, free-electron laser (FEL) science, and materials science, as well as in medical and industrial applications.^{1,2} High-energy accelerators propagate large, radiofrequency (RF) electromagnetic fields within superconducting RF (SRF) cavities to generate and control beams of charged particles.³ These RF fields, however, only penetrate through the first ~ 100 nm of the cavity surface: SRF cavity performance is controlled by the chemistry and quality of the surface.⁴ To lower RF surface

resistance (R_s), minimize power loss, and optimize performance, the surface preparation of the SRF cavity must be designed and implemented carefully.

Oxidized niobium surfaces are the current industry standard for SRF cavities. Nb has the highest critical temperature of elemental superconductors ($T_c = 9.3$ K) and has low RF surface resistance at operating temperatures of about 2 K.^{5–8} Additionally, Nb is thermally conductive and malleable; it can be cooled effectively and formed into SRF cavity shapes.^{5,9} High-energy particle accelerator facilities, such as those at Fermi National Accelerator Lab and the European Council for Nuclear Research (CERN), require

a large series of SRF cavities to produce intense and accelerated beams—these series are up to tens of km in length.^{9–11} Due to their extreme size and an operational temperature (~ 2 K) below helium's boiling point (4.2 K), the accelerators require extremely costly cryocooling systems, maintenance facilities, and staff.^{6,12} Further developments in cavity surface preparation techniques, and even new surface materials, are needed to improve accelerator performance, raise operating temperatures, and lower operational costs.^{1,6,13}

Niobium has a strong affinity for oxygen. When exposed to air, Nb's surface forms an oxide layer that may be altered by temperature treatments but will return persistently, implying that Nb components in accelerators are covered by an oxide layer.^{14,15} Due to the penetration depth of RF fields, changes in the oxide significantly affect the chemistry of SRF cavity treatments and resulting cavity performance.⁴ To gain a thorough and accurate understanding of the interfacial mechanisms driving the performance and development of SRF cavities, we first must investigate the chemistry, structure, and dynamics of oxidized Nb surfaces. The structures of the oxides formed on Nb(100), Nb(110), Nb(111), and polycrystalline Nb have been well characterized, especially at low temperatures.^{15–26} Very recently, helium atom scattering (HAS) and Auger electron spectroscopy (AES) were used to characterize the evolution of an oxide surface at elevated temperatures, showing that the (3×1) -O reconstruction of the Nb(100) surface is stable up to at least 1130 K.²⁷ However, oxide surface dynamics on this material have not yet been reported. The (3×1) -O Nb(100) surface provides an ideal system to begin investigating the chemistry of Nb oxide surfaces, and this study of the surface's phonon band structure provides information needed to refine current and develop new materials for SRF cavities.

Atomic and molecular beam scattering have been used to investigate the structure and vibrational dynamics of surfaces since the 1920s.²⁸ Supersonic He beams are suited to study surfaces due to their lack of penetration into the bulk, inertness, and unusually narrow velocity distributions.^{29–33} Helium atoms' momentum and energy are well matched to those of surface phonons, giving HAS a unique ability to measure and resolve low-energy phonon modes.^{29–35} These modes, particularly the Rayleigh mode, are sensitive to changes in surface interatomic forces and bonding.³⁶ In previous studies, the phonon dispersions of bulk Nb and the bare Nb(100) surface were studied with neutron and He atom scattering, respectively, as well as fit to lattice dynamical calculations.^{37–39} Neutron scattering revealed unusual phonon anomalies for bulk Nb modes along high-symmetry directions.^{37–41} These phonon dispersion curves were best fit by a model that includes electronic degrees of freedom, indicating that the anomalies are caused by electron-phonon coupling (EPC).³⁷ Additionally, Kohn anomalies along low-symmetry directions also point to electron-phonon interactions.^{40,41} The previous HAS study of Nb(100) surface modes shows no such anomalies, but measurements were confined to the first half of the Brillouin zone (BZ) due to experimental limitations. Furthermore, the discrepancy between the force-constant model used and the experimental data prompted the authors to conclude that a first-principles theoretical approach would be needed to describe the surface accurately.³⁷

Unlike for insulators, the interaction between scattered He atoms and the conduction electrons in a metal must play a large

role in any successful theoretical model. The He-surface potential is softened relative to that of ionic crystals, while energy exchange with surface phonons is mediated by surface electrons.³⁶ Density-functional theory (DFT) is a first-principles approach that can create a lattice-dynamical model that includes the role of free electrons in interatomic forces.³⁶ By reframing the quantum many-body problem into an auxiliary system of independent electrons interacting in an effective potential, while treating the atomic nuclei classically, calculating the dynamical matrix and surface phonon dispersions for the (3×1) -O reconstruction of the Nb(100) surface becomes feasible.⁴² In addition, DFT can provide *ab initio* estimates to quantify the extent of the electron-phonon interaction for a given phonon mode, which correlates directly with the intensity of inelastically scattered He for that phonon.³⁶

This combined HAS and DFT study investigates the phonon band structure of the (3×1) -O Nb(100) reconstruction, in addition to the band structures of bulk Nb and the bare Nb(100) surface. The first-principles description of the surface phonon dispersion curves makes clear how the oxide affects phonon polarizations and interatomic forces, and it contributes to a fundamental, chemical understanding of the crystalline and polycrystalline oxidized Nb surfaces. This study provides needed atomic-scale information to the wider SRF community and aids the development of materials for Nb SRF cavities.

II. EXPERIMENTAL

A. Helium atom scattering

We performed measurements with an ultra-high vacuum (UHV) HAS apparatus that provided high angular and energy resolution. A brief overview of the instrument is included here but has been reported in detail elsewhere.⁴³ There are three main regions of the HAS instrument: A differentially pumped beam source, a sample chamber, and a differentially pumped, rotatable detector arm. The He beam was generated by expansion through a $15 \mu\text{m}$ nozzle that was cooled by a closed-cycle He refrigerator. After passing through a skimmer, the beam was modulated by a mechanical chopper before colliding with the Nb surface. The resulting supersonic He beam was nearly monoenergetic ($\Delta v/v \leq 1\%$) and hit the 1 cm sample with a ~ 4 mm spot size. A triply differentially pumped, computer-controlled, rotatable detector arm collected the reflected He atoms. The atoms were ionized by electron bombardment, filtered using a quadrupole mass spectrometer, and detected with an electron multiplier followed by pulse counting electronics. A total He flight path of 1.070 m was used to maximize intensity and resolution. Chopper-to-crystal distance was 0.500 m, with a crystal-to-ionizer distance of 0.571 m.

We took elastic diffraction data with a beam modulated by the chopper in a square-wave pattern, with a 50% duty cycle. Angular distributions were obtained by rotating the detector at 0.2° increments while holding the incident angle and energy fixed, with an overall instrument angular resolution of 0.45° . We collected elastic and inelastic time-of-flight (TOF) spectra by chopping the beam with either a 50% duty cycle for cross-correlation analysis—a pseudorandom 511-bit sequence of openings in the chopper wheel that increases signal-to-noise ratios—or with a single-slit, 1% duty cycle pattern.⁴⁴ TOF spectra often were taken multiple times under

identical conditions and added to form composite spectra with increased signal-to-noise.

The Nb(100) crystal was mounted on a six-axis manipulator within the HAS instrument's sample chamber. This manipulator afforded precise control over the incident angle, θ_i , azimuthal angle, ϕ , and tilt, χ , with respect to the scattering plane. Electron bombardment heating and a closed-cycle He refrigerator modulated the sample temperature within a range of 300 to 1900 K. Surface Preparation Laboratory (the Netherlands) provided the Nb(100) sample (99.99% purity, $\sim 0.1^\circ$ cut accuracy), which we then cleaned in the HAS instrument by cycles of annealing at and flashing to 1900 K, in addition to sputtering with 500 eV Ne⁺ ions (3 μ A maximum). Impurities identified by *in situ* AES were C, B, S, and N; these were removed by the combination of annealing, flashing, and sputtering. We continued the cleaning cycles until only Nb and O were present on the surface, as confirmed by AES, and until the surface was smooth enough for high-intensity He diffraction. Due to the annealing, flashing, and sputtering process described above, the (3 \times 1)-O reconstruction forms naturally and spontaneously. The creation of the oxide has been well documented: when a Nb crystal is annealed or flashed above 600 K, the native, thick, Nb₂O₅ layer reduces to NbO₂ and then NbO.^{45–47} Annealing Nb(100) between 870 and 1970 K causes the (3 \times 1)-O ladder structure to form spontaneously;¹⁶ bare Nb is not seen with anneal temperatures lower than 2500 K.^{16,19} We confirmed the presence of the ladder structure through AES peak ratios, LEED spectra, and HAS. During data collection, the Nb sample periodically was flashed to about 1200 K to eliminate unwanted surface adsorbates.

B. Density-functional theory

We calculated electron and phonon properties of Nb and NbO with DFT using the open-source plane-wave software JDFTx.^{48,49} The electronic states for the outer electrons of Nb (4p⁶5s²4d³) and O (2s²2p⁴) were calculated by treating exchange and correlation effects with the Perdew-Burke-Ernzerhof (PBE)-sol functional and applying the corresponding ultrasoft pseudopotentials parameterized for the functional.^{50,51} All DFT calculations presented in this paper employ an electronic cutoff energy of 20 hartree, with a 200 hartree charge density cutoff. Electronic properties for bulk BCC Nb were calculated by sampling 18³ *k*-points in the Brillouin zone and solving for 15 bands, with electron occupancies corresponding to a Fermi function at an effective electron temperature of 5 mH. With these parameters, we calculated the lattice constant of Nb to be 3.27 Å, in excellent agreement with the experimental measurement of 3.29 Å.¹⁹ The surface calculations for cubic Nb(100) and (3 \times 1)-O Nb(100) sampled 12 \times 12 \times 1 and 3 \times 9 \times 1 *k*-points in the respective Brillouin zones, and electronic occupancies for both systems were calculated using an effective electron temperature of 20 mH. A ten-layer slab was used to calculate the properties of Nb(100) and an asymmetric eight-layer slab was used for (3 \times 1)-O Nb(100), with the oxide on one surface and bare Nb(100) on the opposite surface. Using this asymmetric cell, we tested the bare Nb surface of the (3 \times 1)-O Nb(100) system against the bare, ten-layer Nb(100) slab to ensure that relevant properties converged. To model the experimental oxide surface, whose structure is dominated by a 3 \times 1 motif, we introduced surface lattice vectors that are 3 \times 1 lattice constants across and allowed the surface vectors of the slab to relax.

The surface lattice vectors of the eight-layer (3 \times 1)-O Nb(100) slab relaxed between the lattice constants of bulk Nb (3.29 Å) and NbO (2.99 Å); specifically, to values of 3.21 and 3.14 Å for the threefold and onefold vectors, respectively.¹⁸ The resulting phonon frequencies of the (3 \times 1)-O Nb(100) slab are real-valued, ensuring that our finite system is dynamically stable. To accommodate the minor differences between the DFT and experimental lattice vectors, the reciprocal space plots reported in this paper comparing theory to experiment reference the Brillouin zone in lattice units.

We calculated phonon properties using the finite-difference supercell method, perturbing atoms by ~ 0.4 to $0.5 a_0$ to calculate the real space interatomic force constant matrix directly.⁵² Adequate supercell sizes were 6 \times 6 \times 6 for bulk BCC Nb, 3 \times 3 \times 1 for cubic Nb(100), and 1 \times 3 \times 1 for (3 \times 1)-O Nb(100). Properties of the coupled electron-phonon systems required fine *k*-space samples for accurate calculations of the scattering integrals; we calculated phonon linewidths by transforming into a maximally localized Wannier function (MLWF) basis to densely sample the Brillouin zone with the Monte Carlo method.⁵³

III. THEORETICAL BACKGROUND

Niobium is a conventional superconductor.⁷ Its properties can be described reasonably well within the Bardeen-Cooper-Schrieffer (BCS) theory of superconductivity, and its electrons condense into Cooper pairs via the electron-phonon coupling (EPC) mechanism.⁵⁴ Theoretical predictions are improved by applying the higher order Eliashberg theory within a DFT framework to calculate EPC explicitly.^{52,55,56} By transforming into an MLWF basis, we calculate directly how electrons couple to various lattice distortions to extract the quantities relevant in predicting inelastic He-scattering rates.⁵⁷ Specifically, we employ perturbation theory and calculate the overlap of the perturbing electron-ion potential between the unperturbed electronic states in order to calculate explicitly the electron-phonon matrix elements within DFT,⁵⁸

$$g_{nk,n'k+q}^{qv} = \left(\frac{\hbar}{2M\omega_{qv}} \right)^{\frac{1}{2}} \left\langle \psi_{n',k+q} \left| \frac{dV^{e-i}}{du_{qv}} \cdot \hat{\epsilon}_{qv} \right| \psi_{n,k} \right\rangle, \quad (1)$$

where u_{qv} and ω_{qv} are the atomic displacements and frequencies, respectively, for the phonon mode ν with crystal momentum \mathbf{q} and polarization vector $\hat{\epsilon}_{qv}$, and M is the ion mass.

The above matrix elements connect to inelastic He-scattering rates through the phonon linewidths and the dimensionless EPC constants. Specifically, the phonon linewidths, or equivalently, the inverse phonon lifetimes, are defined as⁵⁹

$$\gamma_{qv} = 2\pi\omega_{qv} \sum_{n,n'} \int \frac{d^3k}{(2\pi)^3} \left| g_{nk,n'k+q}^{qv} \right|^2 \delta(e_{q,n} - e_F) \delta(e_{k+q,n'} - e_F). \quad (2)$$

These linewidths then determine the dimensionless EPC constants,

$$\lambda_{qv} = \frac{\gamma_{qv}}{\pi\hbar N(e_F)\omega_{qv}^2}, \quad (3)$$

where $N(e_F)$ denotes the electronic density of states (DOS) at the Fermi level.

Finally, to estimate HAS signal intensities, we follow the theoretical frame of Benedek *et al.* and estimate the inelastic scattering probability to be proportional to λ_{qv} , but instead of using an approximate analytic form for the surface electron-phonon matrix elements, we calculate the matrix elements *ab initio* directly in an MLWF basis using DFT.^{60–64} In order to better probe the surface-specific phonon characteristics measured by HAS, we project the mode-selected EPC constants onto the z -displacements of the corresponding phonon polarization vector, while including the exponential decay of the He wave functions into the material, and define the surface-projected EPC constants as

$$\bar{\lambda}_{Qv} \propto \sum_{Qv,\kappa} |e^{\alpha=z}(\mathbf{Qv})|^2 \lambda_{Qv} \exp(-\beta z_\kappa) \delta(E - \hbar\omega_{Qv}). \quad (4)$$

Here, κ labels the atoms, z represents the atoms' distance beneath the surface, β is the He decay softness parameter, and E is the energy transfer of the He atom. The above expression is written as a proportionality because here we do not include factors, such as additional matrix elements, that are considered to be energy- and wavevector-independent.^{60–63} Following standard distorted-wave Born approximations of atom-surface potentials, we estimate the softness parameter, β , for Nb(100) to be $\sim 2.1 \text{ \AA}^{-1}$, which falls within the typical range expected for metals.^{36,65}

IV. RESULTS AND DISCUSSION

Helium diffraction scans from the $(3 \times 1)\text{-O}$ Nb(100) surface are shown in Fig. 1. Figure 1(a) is a representative angular scan along

the $\langle \bar{1}00 \rangle$, $\bar{\Gamma}\bar{X}$ azimuthal direction, while Fig. 1(b) is a scan along the $\langle \bar{1}10 \rangle$, $\bar{\Gamma}\bar{M}$ direction with an inset diagram of the reciprocal surface lattice vectors. We took both scans with a cold He beam ($E_i = 21 \text{ meV}$ and slightly elevated surface temperatures [$T_s = 360$ and 410 K for Figs. 1(a) and 1(b), respectively]). The scan in Fig. 1(a) was taken at an incident angle of $\theta_i = 34.8^\circ$; we confirmed surface reproducibility by taking repeated diffraction scans at $T_s = 360 \text{ K}$ after flashing the crystal to 1200 K . The specular peak ($\theta_i = \theta_f$) at $\Delta K = 0$ is ~ 2.6 times more intense than the next largest, first-order $(0\bar{1})$ diffraction peak at $\Delta K = -1.9 \text{ \AA}^{-1}$ ($\theta_f = 15.8^\circ$). When compared with a scan of bare Nb(100), the larger first- to zeroth-order peak intensity ratio indicates that the oxide structure has a higher surface corrugation.³⁵ In particular, we note that the first-order diffraction peak intensity is within the same order of magnitude as the specular intensity, while the first-order diffraction intensity observed for the bare Nb(100) surface is over two orders of magnitude less than the specular intensity.³⁷ Each peak occurs when the Bragg equation holds true; that is, when

$$\Delta K = k_i(\sin \theta_i - \sin \theta_f) = G_{mn}, \quad (5)$$

where the surface-parallel component of the He wavevector k_i changes by ΔK ; the initial and final scattering angles, relative to surface normal, are θ_i and θ_f , respectively; and G_{mn} is a linear combination of reciprocal surface lattice vectors.

Three additional diffraction peaks are visible in the angular scan of the $\langle \bar{1}00 \rangle$, $\bar{\Gamma}\bar{X}$ azimuthal direction, all of which correspond to the $(3 \times 1)\text{-O}$ ladder structure. The $(0\frac{1}{3})$ peak, at $\Delta K = -0.6 \text{ \AA}^{-1}$ ($\theta_f = 28.7^\circ$), is approximately one-third of the way between the (00)

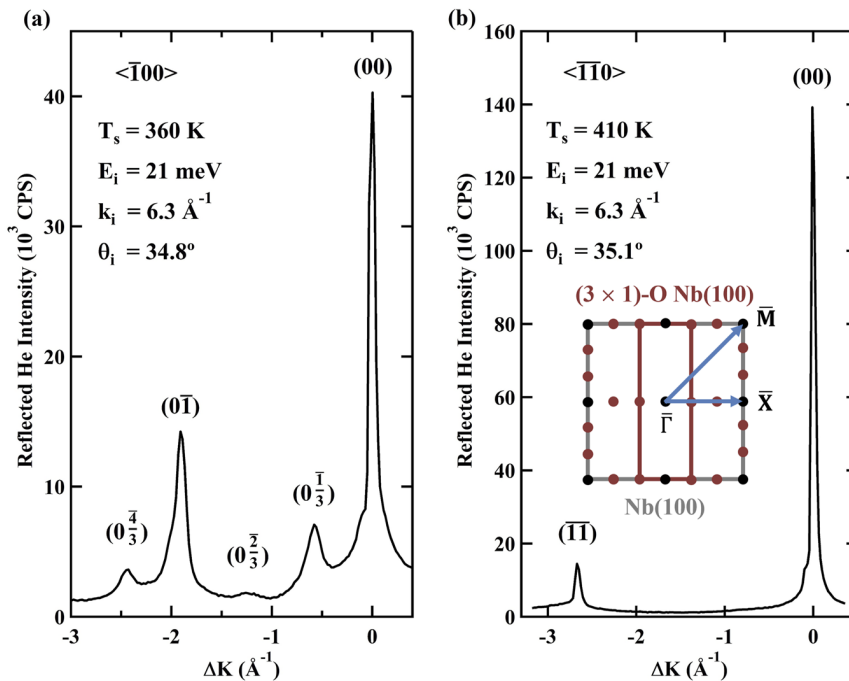


FIG. 1. Representative He atom diffraction spectra for the $(3 \times 1)\text{-O}$ Nb(100) surface along the (a) $\langle \bar{1}00 \rangle$ and (b) $\langle \bar{1}10 \rangle$ symmetry axes, with the inset diagram in (b) showing the reciprocal surface lattice vectors. The specular (00) peak is visible in both directions, while the oxide structure can be seen in (a) along the $\langle \bar{1}00 \rangle$ axis, with fractional peak notation corresponding to the $(3 \times 1)\text{-O}$ structure. The $\langle \bar{1}10 \rangle$ axis in (b) shows the underlying $\bar{1}10$ Nb(100) lattice peak.

and $(0\bar{1})$ peaks. Similarly, the $(0\frac{2}{3})$ peak ($\Delta K = -1.2 \text{ \AA}^{-1}$, $\theta_f = 22.0^\circ$) is two-thirds of the way between the primary peaks, while the $(0\frac{4}{3})$ peak ($\Delta K = -2.4 \text{ \AA}^{-1}$, $\theta_f = 10.8^\circ$) is past the $(0\bar{1})$ peak by one-third of that distance. The visibility of all three superlattice peaks shows the excellent surface order of the sample and the minimal scattered He background intensity measured by the detector.

The angular scan in Fig. 1(b) was taken at an incident angle of $\theta_i = 35.1^\circ$ in the $\langle\bar{1}10\rangle$, $\bar{\Gamma}\bar{M}$ direction. Since the (3×1) -O reconstruction does not affect atomic spacing along this azimuthal direction, only primary lattice diffraction peaks are seen. The specular peak at $\Delta K = 0$ is much larger than the first-order, $(\bar{1}1)$ diffraction peak ($\Delta K = -2.7 \text{ \AA}^{-1}$, $\theta_f = 8.9^\circ$), indicating that the surface is corrugated slightly less along this axis than along the $\bar{\Gamma}\bar{X}$ axis.³⁵

For inelastic, in-plane scattering, the conservation of energy and crystal momentum dictates possible scattering angles and energies. For a given beam with incident energy E_i , wavevector k_i , and angle θ_i , possible final conditions (angle θ_f , wavevector k_f , and energy E_f) must satisfy the following equation:

$$\Delta K = k_f \sin \theta_f - k_i \sin \theta_i = G_{mn} + Q, \quad (6)$$

where G_{mn} again is a linear combination of reciprocal surface lattice vectors and Q is the two-dimensional wavevector for a phonon with energy $\hbar\omega$. By substituting relevant energies [Eq. (7)] and rearranging, the scan curve indicating accessible phonons can be extracted [Eq. (8)],

$$\Delta E = E_f - E_i = \frac{\hbar^2 k_f^2}{2m} - \frac{\hbar^2 k_i^2}{2m} = \hbar\omega(Q), \quad (7)$$

$$\frac{\Delta E}{E_i} = \frac{(\sin \theta_i - \frac{\Delta K}{k_i})^2}{\sin^2 \theta_f} - 1. \quad (8)$$

Systematically varying incident beam energy and angle while capturing TOF spectra moves the scan curve across the surface Brillouin zone (SBZ) and maps out surface phonon resonances.

Figure 2 shows examples of cross-correlation TOF spectra measured along the $\langle\bar{1}00\rangle$, $\bar{\Gamma}\bar{X}$ axis. Each spectrum was taken under specific incident and final conditions that maximized intensity and resolution. We explored various surface temperatures, with $T_S = 670 \text{ K}$ yielding the best results: for this axis, all spectra were taken with cross-correlation chopping at $T_S = 670 \text{ K}$. Figures 2(a) and 2(b) were taken with incident energies $E_i = 16$ and 21 meV and angles $\theta_i = 27.2^\circ$ and 34.7° , respectively. The dominant peak in each spectrum is elastic, where $E_i = E_f$, and was used to calculate incident beam energy. Subsidiary peaks—indicated by black arrows—are phonon modes, with peaks to the left of elastic corresponding to surface phonon annihilation (the He beam gains energy), and peaks to the right corresponding to surface phonon creation (the He beam loses energy). We identified the position of the top of each peak by fitting a given spectrum with multiple Gaussian functions and extracting the function centers. That time then was correlated with a specific ΔE and ΔK for the He beam and plotted, along with the corresponding scan curve, in the insets of Fig. 2.

Figure 3 shows similar TOF spectra but taken along the $\langle\bar{1}10\rangle$, $\bar{\Gamma}\bar{M}$ axis. Along this axis, we held the surface temperature at either $T_S = 300$ or 410 K , depending on the scan. Additionally, a few phonon modes identified in this direction were measured using a single-shot chopping pattern for increased resolution, though Fig. 3 contains cross-correlation data. Figure 3(a) was taken with $T_S = 410 \text{ K}$, $E_i = 10 \text{ meV}$, and $\theta_i = 21.1^\circ$, while $T_S = 300 \text{ K}$,

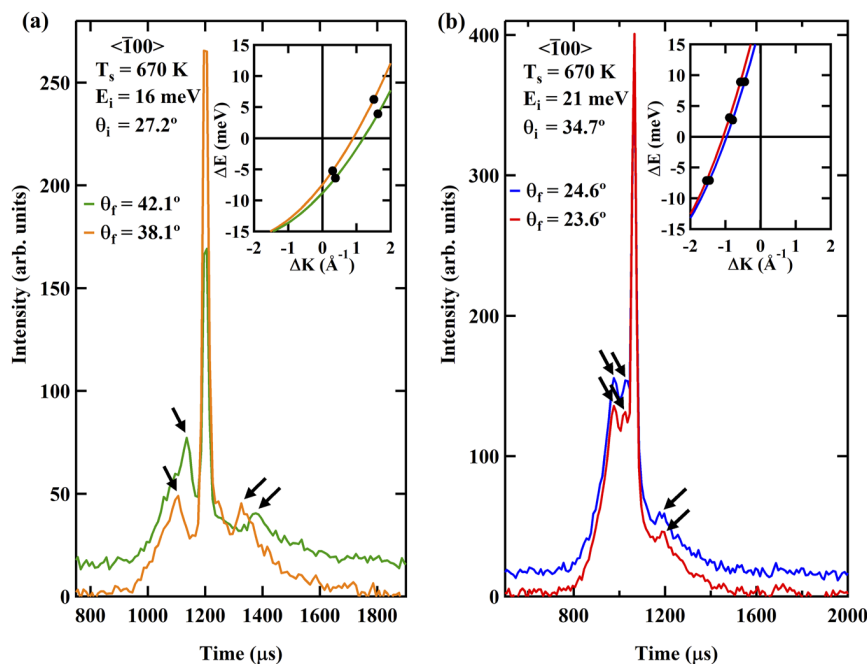


FIG. 2. Representative cross-correlation TOF spectra for the (3×1) -O Nb(100) surface along the $\langle\bar{1}00\rangle$ symmetry axis, under different incident and final conditions. Data in (a) were taken with a 16 meV incident He beam, while data in (b) were taken with a 21 meV incident beam. Phonon peaks are designated by black arrows, with insets showing representative scan curves for each spectrum. Black dots indicate phonon peak positions; ΔE is the energy gained or lost by the He beam.

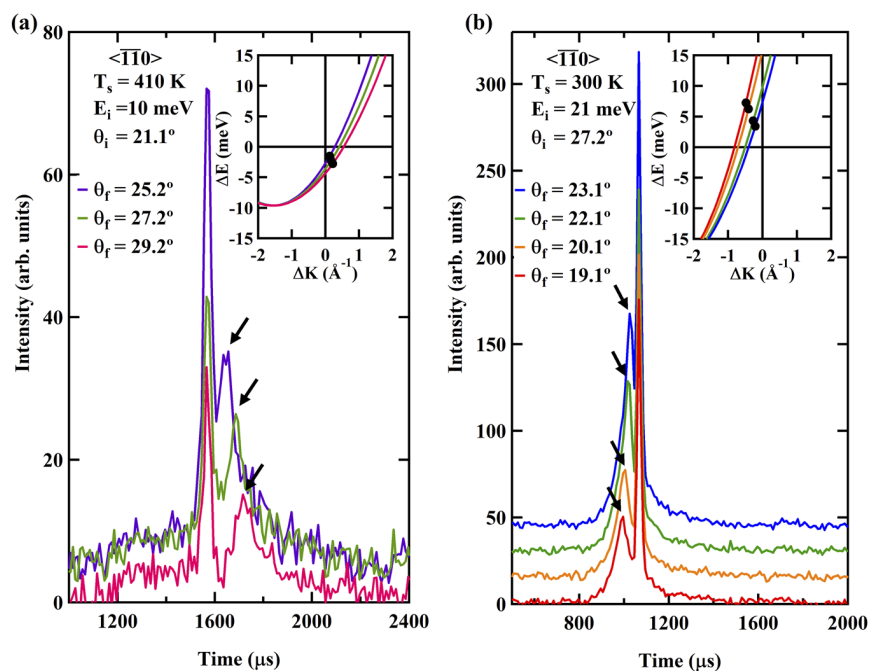


FIG. 3. Representative cross-correlation TOF spectra for the (3×1) -O Nb(100) surface along the $\langle \bar{1}10 \rangle$ symmetry axis. Data in (a) were taken with a 10 meV incident He beam, while data in (b) were taken with a 21 meV incident beam. Phonon peaks are designated by black arrows; insets show representative scan curves for each spectrum with black dots indicating phonon peak positions. ΔE is the energy gained or lost by the He beam.

$E_i = 21$ meV, and $\theta_i = 27.2^\circ$ for Fig. 3(b). Phonons are identified with black arrows and we obtained peak positions in the same manner as for Fig. 2. Phonon positions in the SBZ with corresponding scan curves are shown in the figure insets.

All measured phonon peak positions are shown in Fig. 4, with Fig. 4(a) showing data taken along the $\bar{1}X$ axis and Fig. 4(b) along the

$\bar{1}M$ axis. As in Figs. 2 and 3, these extended SBZs are as measured by the He beam, with ΔE indicating energy gained or lost by the beam. Multiple phonon resonances are seen in both axes and will be discussed below with DFT results.

Figure 5(a) shows the DFT-calculated phonon modes of bulk Nb along the BCC Brillouin zone symmetry directions (colormap)

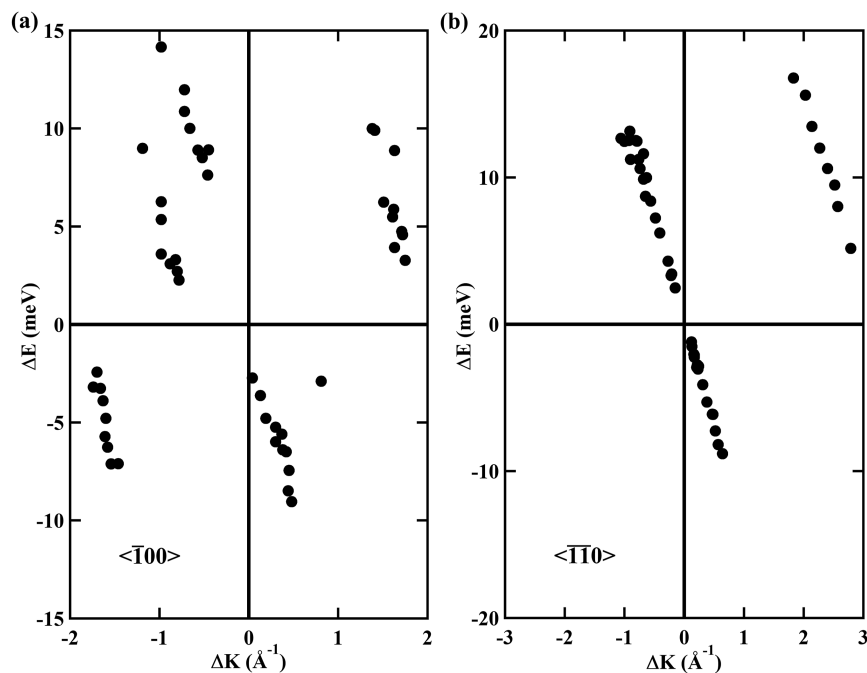


FIG. 4. Extended dispersion plots along the (a) $\langle \bar{1}00 \rangle$ and (b) $\langle \bar{1}10 \rangle$ symmetry axes. Each point corresponds with the center of a phonon peak from a TOF spectrum. These values are as measured by the He beam, where ΔE indicates energy gained or lost by the He beam.

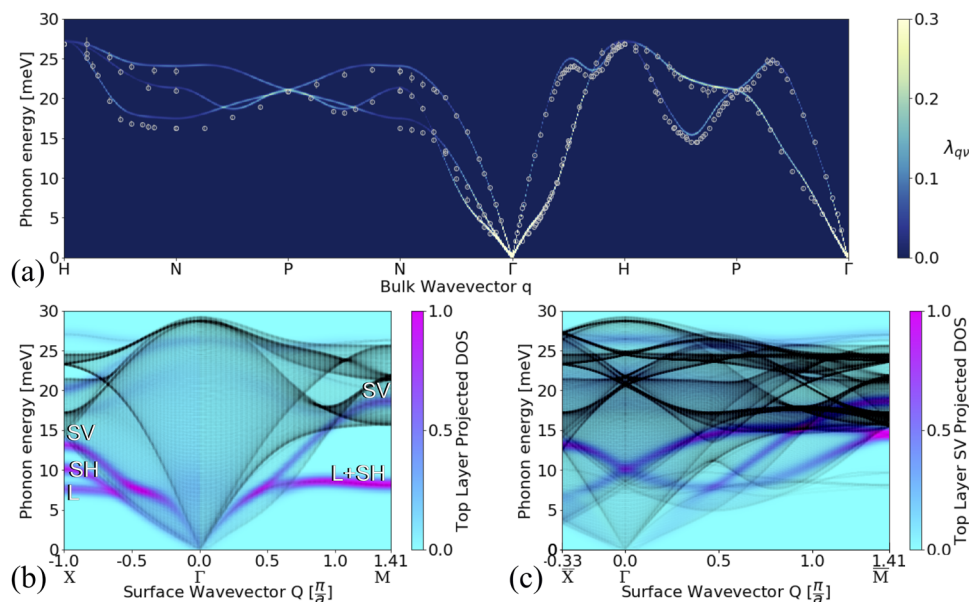


FIG. 5. (a) Bulk phonon dispersions calculated for Nb along high-symmetry paths of the BCC Brillouin zone, where each mode's EPC strength is indicated by its brightness level and brighter colors correspond to stronger coupling. Neutron scattering data from literature (white circles) are overlaid on the calculations for comparison.³⁸ Surface phonons along symmetry directions $\Gamma\bar{X}$ and $\Gamma\bar{M}$ for (b) cubic Nb(100) and for (c) (3×1) -folded Nb(100). Black lines represent phonon dispersions calculated for an effective 130-layer slab of Nb(100). The colormaps display the surface phonon density of states (DOS) projected onto the top layer of atoms, and surface resonances are labeled for the shear-vertical (SV), shear-horizontal (SH), or longitudinal (L) in (b). The (3×1) -folded Nb(100) colormap in (c) displays only the SV mode to demonstrate the BZ folding process more clearly.

compared with neutron scattering data from literature (white circles).³⁸ The DFT-calculated modes reproduce previously calculated and measured results, confirming the accuracy of the method used.^{37,38} Phonon anomalies indicated by the change in slope of the bottom-most resonances along the $\Gamma\bar{H}$ and $\Gamma\bar{N}$ directions are observed, as are dips in the higher resonance along $\Gamma\bar{H}$ and lower resonance along $\Gamma\bar{P}$, and a resonance crossing near H along $\Gamma\bar{H}$.^{37,39} The bulk phonon modes are colored by their respective EPC constant strengths, λ_{qv} : by taking advantage of the MLWF basis, we are able to track the EPC of bulk Nb throughout the Brillouin zone. The strongest coupling is seen near the Γ point for all resonances, which corresponds with lower phonon energies.

Next, we identified both surface-projected bulk phonon modes and surface modes for an effective 130-layer slab of Nb(100) by beginning with a ten-layer slab and inserting 120 bulk layers into its dynamical matrix. These results are shown in Fig. 5(b) along symmetry directions $\Gamma\bar{X}$ and $\Gamma\bar{M}$ and are overlaid with a colormap of the top-layer surface phonon density of states (DOS). By examining the atomic displacements associated with the surface phonon modes, we identify polarizations and find that the longitudinal (L) and shear-horizontal (SH) modes dip below the shear-vertical (SV) mode and the bulk-projected band along both symmetry directions. The highest surface DOS is seen in the L + SH mode near \bar{M} . In Fig. 5(c), we folded the effective 130-layer slab of cubic Nb(100) to represent a (3×1) -folded BZ equivalent to the BZ of (3×1) -O Nb(100). The folded BZ displays more apparent resonances at a given wavevector, both surface-projected bulk and strictly surface,

as a result of the folding. For example, what once were acoustic modes can now, after folding, appear as optical modes. This process is illustrated in Fig. 5(c): considering only the top-layer SV projected DOS for clarity, the DOS now disperses to higher phonon energies at shorter wavevectors. Accordingly, surface modes are folded to near the middle of the surface-projected bulk band, and the SV mode, in particular, is translated to about 10 meV at the $\bar{\Gamma}$ -point.

Figure 6 shows the results from our calculated EPC strengths for bulk Nb projected onto the (100) SBZ, along with the coupling strengths for the bare Nb(100) and (3×1) -O Nb(100) surfaces. Values of surface EPC strengths are projected onto exponentially weighted z -displacements [see Eq. (4)], as these are what can be seen most readily with HAS. The first BZ for both the bare and (3×1) -O surfaces are folded to correspond with the ladder structure and allow for direct comparison. The EPC for the Nb(100) surface is pronounced near the $\bar{\Gamma}$ -point at low energies and near 11 meV, higher than it is for bulk Nb projected on the SBZ. Multiple resonances are seen along both directions for Nb(100), though most of the EPC strength is concentrated below 16 meV.

The electron-phonon interaction strength becomes much more dispersed for the oxide surface, with multiple new resonances appearing at higher phonon energies due to the addition of the less massive O atoms. The resonances at $\bar{\Gamma}$, ~ 11 meV for Nb(100) move higher, to about 13 meV, and lose significant relative strength for the oxide. The resonance at 7 meV appears more intense for the oxide, as are the lowest resonances along both symmetry directions. High-energy, optical modes also appear in the oxide, most notably

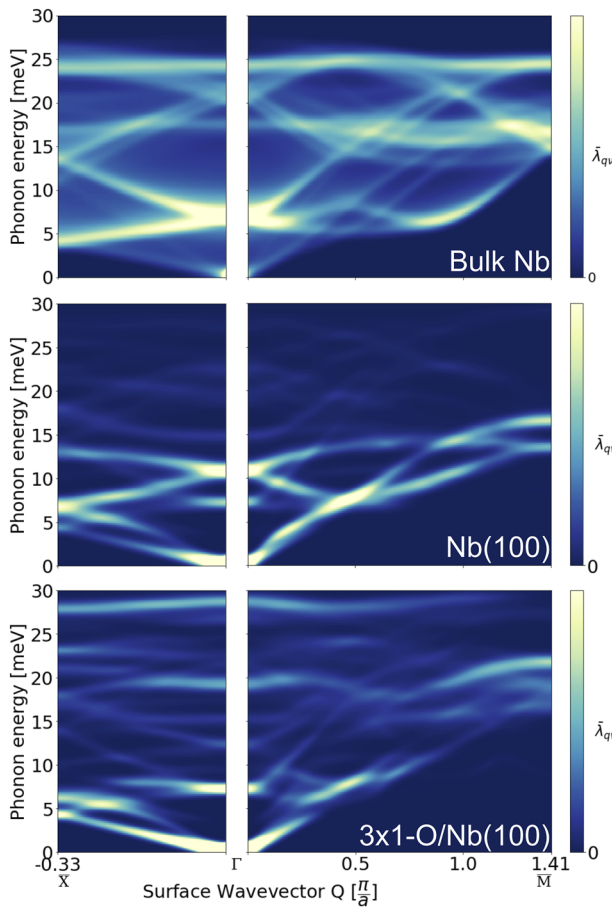


FIG. 6. Surface EPC strengths along SBZ symmetry directions $\overline{\Gamma X}$ (left column) and $\overline{\Gamma M}$ (right column), projected from bulk Nb (top row) onto the SBZ and projected onto the exponentially weighted z-displacements using Eq. (4) for (middle row) the bare Nb(100) surface and (bottom row) the (3×1) -O Nb(100) surface. Coupling strengths are indicated by brightness level, with brighter colors corresponding to stronger coupling.

near 28 meV. However, the strongest couplings for the bare Nb(100) and oxide surfaces are seen in approximately the same locations: in the acoustic modes near the $\overline{\Gamma}$ point for 0–3 meV; near the \overline{X} point around 5 meV; and near $0.5 \pi/a$ along $\overline{\Gamma M}$ around 7 meV.

When a He atom scatters from a metal, it interacts with the surface electron density. The creation or annihilation of surface phonons occurs through these electrons, intrinsically linking HAS with EPC strengths.³⁶ In Fig. 7, HAS phonon data are overlaid on the calculated dispersion plot for (3×1) -O Nb(100), where experimental data points are shown as white dots and EPC strength is indicated by brightness. Satisfactory agreement is seen between the experimental and theoretical results and demonstrates the importance of electron-phonon interactions in resonances visible with inelastic He scattering. The density of measured points is a convolution of experimental conditions and available phonon modes—where phonons were more easily resolved, more phonons

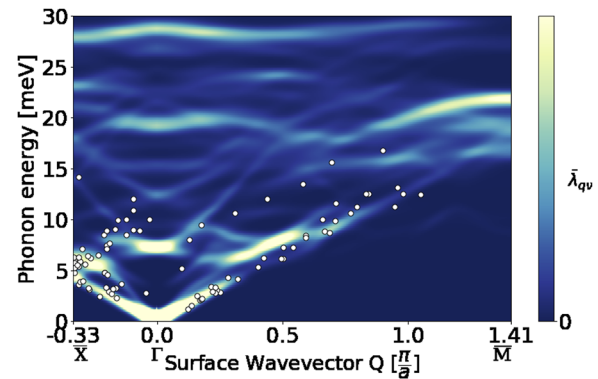


FIG. 7. Phonons for the (3×1) -O Nb(100) surface measured with HAS (white dots), overlaid on DFT-calculated surface EPC strengths projected onto z-displacements, using Eq. (4). Coupling strengths are indicated by brightness level, with brighter colors corresponding to stronger coupling. HAS data and theoretical predictions along $\overline{\Gamma M}$ were translated back into the first BZ of cubic Nb(100), while the data along $\overline{\Gamma X}$ was folded back to the (3×1) -folded BZ of the ladder structure.

were measured. The highest density of measured points, near \overline{X} around 6 meV and near $0.25 \pi/a$ along $\overline{\Gamma M}$ around 3 meV, corresponds well with the stronger EPC calculated by DFT. Along the $\overline{\Gamma X}$ direction two acoustic modes can be seen with HAS, though their distinction is blurred at higher energies by the folding of the first BZ. The lowest mode is the Rayleigh mode while the upper is longitudinal, but as will be seen in Fig. 8, towards the zone boundary there is a hybridization and mixing of SV and L displacements which blurs this distinction, a common feature of metal surfaces.⁶⁶

There also are two modes measured with HAS along the $\overline{\Gamma M}$ direction, with the lower mode again being the Rayleigh mode. By comparing the EPC strengths for Nb(100) and (3×1) -O Nb(100) in Fig. 6, we attribute the upper measured mode primarily to the addition of the oxide on the surface. This corresponds with the trend seen in Fig. 6, where the oxide disperses EPC, and hence inelastic He-scattering intensity, to higher energies. An anomalous feature can be seen in the lowest longitudinal mode along $\overline{\Gamma M}$, indicating a lattice instability, which often is accompanied by a symmetry breaking and may be related to the oxide reconstruction, but requires further analysis.⁶⁷

By comparing our experimental data for the (3×1) -O Nb(100) surface with data from literature for the bare, Nb(100) surface, we see changes caused by the oxide reconstruction.³⁷ Our data and that from Hulpke *et al.* both show two measured modes along $\overline{\Gamma X}$ and $\overline{\Gamma M}$.³⁷ Along $\overline{\Gamma X}$, these modes agree between the two surfaces, though our data extends much farther into the first SBZ, limiting the comparison. Along $\overline{\Gamma M}$, however, the high-energy mode is significantly stiffened for the oxide surface. This increase in energy ranges from about 2 to 4 meV: larger differences are seen closer to $\overline{\Gamma}$, while the difference decreases somewhat as the mode disperses through the BZ. As will be seen in Fig. 9, the stiffening of the phonon mode corresponds with increased surface force constants for the oxide and indicates that the oxide stabilizes the Nb(100) surface. The lower, Rayleigh mode measured along $\overline{\Gamma M}$ appears to follow that measured for metallic Nb, but as with the $\overline{\Gamma X}$ direction, the data from Hulpke

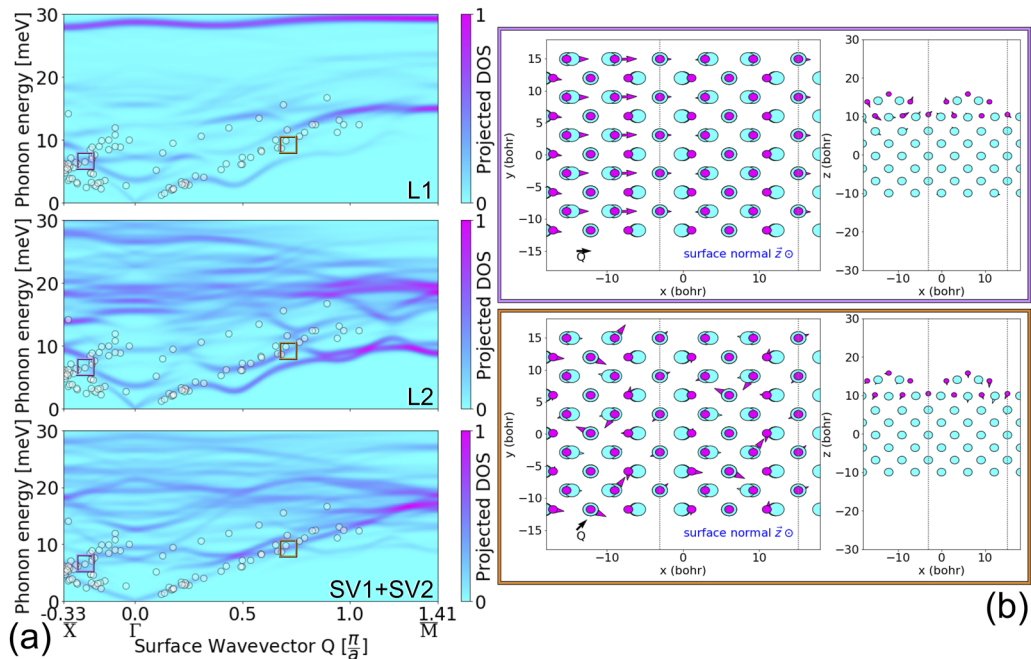


FIG. 8. Top layer densities of states projected onto the SV or L displacements of the surface atoms of (3×1) -O Nb(100); from top to bottom: L displacements from layer 1 (L1) and from layer 2 (L2), and SV displacements from layers 1 and 2 (SV1 + SV2), where layer 1 refers to the crest of the oxide and layer 2 denotes the planarly intact layer beneath the crest. Each white circle marks an HAS event (repeated from Fig. 7). (b) Atomic displacements of the Nb atoms (larger teal circles) and O atoms (smaller magenta circles) for (3×1) -O Nb(100) calculated with DFT corresponding to the two boxed modes highlighted in (a). The displacements in the (upper) violet box correspond to the mode along $\overline{\Gamma X}$ at 6.8 meV and the displacements in the (lower) orange box correspond to the mode along $\overline{\Gamma M}$ at 9.3 meV. The arrows in (b) indicate directions of the atomic displacements and their relative magnitudes, viewing (left) down along surface normal and viewing (right) along the surface with the surface normal pointing up. The vertical dashed lines in (b) coincide with the troughs in the ladder structure.

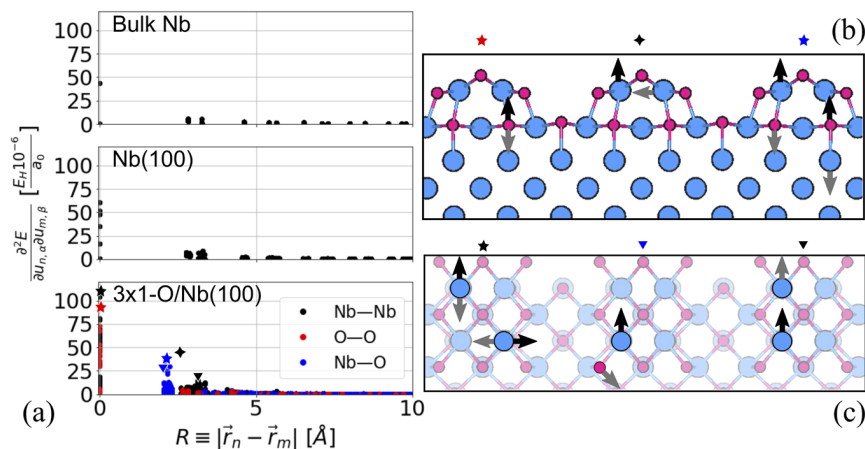


FIG. 9. (a) Pairwise interatomic force constants in bulk Nb, Nb(100), and (3×1) -O Nb(100) all plotted on the same scale as a function of distance between the two atoms, with $R = 0$ corresponding to the force on an atom when it is perturbed. All interatomic force constants in bulk Nb and Nb(100) involve only Nb–Nb interactions (black circles), while (3×1) -O Nb(100) includes additional force constants between Nb–O (blue circles) and O–O (red circles). Noteworthy interatomic force constants in (3×1) -O Nb(100) are marked with distinct symbol shapes in (a) and then depicted in the crystal structures in either (b) a side view with surface normal pointing up or in (c) a top down view with surface normal pointing out of the page. In (b) and (c), Nb atoms are colored as larger blue circles and O as smaller magenta circles, and the black and gray arrows correspond to the atomic perturbation and responding forces, respectively.

et al. do not extend far into the first SBZ, and we are not able to compare data near the \bar{M} zone edge, though this is where the DFT-calculated Rayleigh wave appears to differ most between the two surfaces in Fig. 6.³⁷

Figure 8(a) shows the top layer DOS projected onto the SV or L displacements of (3×1) -O Nb(100) surface atoms. This projection allows us to assign polarizations to the modes measured by HAS. Along $\bar{\Gamma X}$, the lowest measured mode, or the Rayleigh mode, is almost entirely SV, while the higher modes are mixed L and SV. Along $\bar{\Gamma M}$, both measured modes appear mixed, though the higher mode is primarily L due to second-layer atoms (L2), while the lower mode mixes L1, L2, and SV1 + SV2. The high-energy optical mode across the entire SBZ is seen to be almost entirely L due to the top layer of atoms—from the crests of the (3×1) -O Nb(100) ladder structure. This mode has the highest DOS for L1, has very little dispersion, and is near the top of the bulk-projected band seen in Fig. 5(c).

Two specific phonons measured by HAS are examined in Fig. 8(b): one along $\bar{\Gamma X}$ (upper violet box) and one along $\bar{\Gamma M}$ (lower orange box). Figure 8(b) shows the atomic displacement directions and magnitudes with arrows corresponding to O (smaller magenta circles) or Nb (larger teal circles) atoms, viewed along surface normal and viewed head-on with surface normal pointing up. For both phonons, the O atoms are much more active than the Nb. The phonon in the violet box is primarily L in the first layer of atoms, as indicated both by Fig. 8(a) and by the direction of the arrows in Fig. 8(b). The resonance in the orange box is a hybridization of L and SV, involving L displacements in the second layer of atoms and SV in both the first and second layers.

Figure 9 shows the pairwise interatomic force constants for bulk Nb, Nb(100), and (3×1) -O Nb(100). The addition of the oxide to the surface causes a significant increase in force constants, even between Nb atoms. The highest force recorded was the force on a Nb atom when it was perturbed along the surface, which is labeled by a black, five-pointed star and illustrated in Fig. 9(c). This force is almost twice the highest force seen for the bare Nb(100) surface, indicating that the oxide stabilizes the surface. Another notable feature is the Nb–Nb force increase caused by the oxide, which is labeled by the black, four-pointed star at approximately $R = 2.6$ Å. This is the surface-parallel force on one of the Nb atoms in the crest of the (3×1) -O Nb(100) ladder structure when another atom in the crest is disturbed along the surface-normal direction, as seen in Fig. 9(b). A surface-parallel perturbation of a Nb atom within the crest causes a relatively high response in a neighboring Nb atom 3.1 Å away, also in the surface-parallel direction [black triangle in Fig. 9(c)]. Most of the force constants that involve O atoms, shown by the red and blue markers in Fig. 9(a), are higher than the Nb–Nb force constants in bulk Nb and the bare Nb(100) surface. This feature occurs most prominently when Nb and O are near neighbors, separated by about $R = 2.1$ Å [blue five-pointed star in Fig. 9(b) and blue triangle in Fig. 9(c)].

Our work shows that the (3×1) -O superlattice structure significantly modifies the forces of bulk Nb and the unreconstructed, bare Nb(100) surface. The strong bonds introduced by the (3×1) -O superlattice make up the characteristic ladder crests and strongly oppose surface-normal and surface-parallel perturbations. This result explains the high-energy phonon resonances in the dispersion plot shown in Fig. 7 and stabilizes the Nb surface, leading

to Nb's strong affinity for O.^{14,15} Additionally, the strengthened Nb–Nb bonds indicate a heightened Nb diffusion barrier at the surface.⁶⁸ The (3×1) -O structure could inhibit nucleation and alloying at the surface, raising surface melting temperatures and the alloying temperatures of relevant SRF materials such as Sn.^{69–71}

Recent work by Farber *et al.* characterizes Sn adsorption and diffusion behavior on the (3×1) -O Nb(100) surface reconstruction.⁷² Their results reveal that defects do not alter significantly either Sn adsorption or diffusion: these processes likely are dictated by the (3×1) -O superlattice structure. Our results support this interpretation of their data by indicating that the ladder crest features are strongly bonded and thus resistant to perturbation. Our results also explain their observed adsorption sites and preferential diffusion along the troughs of the ladder structure. An atomic-scale, theoretical characterization of the (3×1) -O Nb(100) surface alloying with Sn has not been completed. However, our results suggest that the ladder troughs are susceptible sites for reactivity or alteration, while the ladder crests are strongly stabilizing and provide a barrier to treatments and corresponding reactions. Further atomic-scale studies of alloying on these surfaces will provide a more detailed picture.

V. CONCLUSION

We used HAS and DFT to map the surface phonon dispersions of the (3×1) -O Nb(100) reconstruction. A comparison between calculated resonances of the bare Nb(100) surface and the oxide surface show a large increase in phonon modes for the oxide, especially at higher energies. We calculated explicitly the electron-phonon interaction strengths at the surface and compared the results with inelastic He TOF data. The agreement seen between experiment and theory allows us to identify the measured surface modes. The primary modes measured with HAS are caused largely by longitudinal and shear-vertical displacements of the top two layers of O and Nb atoms on the (3×1) -O surface, and these modes also display meaningful electron-phonon interaction strengths. The DFT analysis of the force constants at the surface show significant increases in bonding between Nb atoms as well as strong Nb–O and O–O bonds. These data further expound what is known about the oxide surface and will inform the development of new SRF materials by elucidating the dynamics of the oxide surface. While this collaborative work begins to reveal how the (3×1) -O superlattice structure alters EPC at the Nb(100) surface, it is only a piece of the picture. Beyond the differences in phonon resonances shown above, the significant modification of interatomic interactions could in turn affect surface superconductivity and SRF cavity behavior. Future experimental and theoretical studies investigating the EPC of these surfaces are currently underway.

ACKNOWLEDGMENTS

S.J.S. and T.A.A. would like to acknowledge support from the U.S. National Science Foundation under Award No. PHY-1549132, the Center for Bright Beams, while S.J.S. also acknowledges support from the Air Force Office of Scientific Research, Grant No. FA9550-19-1-0324, for fundamental studies of gas-surface energy transfer. Support from the NSF-Materials Research Science and Engineering

Center at the University of Chicago (Grant No. NSF-DMR-2011854) is also acknowledged.

AUTHOR DECLARATIONS

Conflict of Interest

The authors declare no competing financial interest.

DATA AVAILABILITY

The data that support the findings of this study are available within the article.

REFERENCES

- 1 A. Grassellino, A. Romanenko, D. Sergatskov, O. Melnychuk, Y. Trenikhina, A. Crawford, A. Rowe, M. Wong, T. Khabiboulline, and F. Barkov, *Supercond. Sci. Technol.* **26**, 102001 (2013).
- 2 R. W. Hamm and M. E. Hamm, *Industrial Accelerators and Their Applications* (World Scientific, Singapore, 2012).
- 3 H. Padamsee, K. W. Shepard, and R. Sundelin, *Annu. Rev. Nucl. Part. Sci.* **43**, 635 (1993).
- 4 D. C. Ford, L. D. Cooley, and D. N. Seidman, *Supercond. Sci. Technol.* **26**, 105003 (2013).
- 5 H. Padamsee, *Supercond. Sci. Technol.* **14**, R28 (2001).
- 6 S. Posen and D. L. Hall, *Supercond. Sci. Technol.* **30**, 033004 (2017).
- 7 D. K. Finnemore, T. F. Stromberg, and C. A. Swenson, *Phys. Rev.* **149**, 231 (1966).
- 8 A. Grassellino, A. Romanenko, Y. Trenikhina, M. Checchin, M. Martinello, O. S. Melnychuk, S. Chandrasekaran, D. A. Sergatskov, S. Posen, A. C. Crawford, S. Aderhold, and D. Bice, *Supercond. Sci. Technol.* **30**, 094004 (2017).
- 9 H. Padamsee, J. Knobloch, and T. Hays, *RF Superconductivity for Accelerators* (Wiley-VCH, New York, 2008).
- 10 F. Gerigk, *IEEE Trans. Appl. Supercond.* **28**, 3500205 (2018).
- 11 D. Broemmelsiek, B. Chase, D. Edstrom, E. Harms, J. Leibfritz, S. Nagaitsev, Y. Pischalnikov, A. Romanov, J. Ruan, W. Schappert, V. Shiltsev, R. Thurman-Keup, and A. Valishev, *New J. Phys.* **20**, 113018 (2018).
- 12 P. Dhakal, G. Ciovati, P. Kneisel, and G. R. Myneni, *IEEE Trans. Appl. Supercond.* **25**, 3500104 (2015).
- 13 S. Posen and M. Liepe, *Phys. Rev. Spec. Top.—Accel. Beams* **17**, 112001 (2014).
- 14 H. H. Farrell, H. S. Isaacs, and M. Strongin, *Surf. Sci.* **38**, 31 (1973).
- 15 H. H. Farrell and M. Strongin, *Surf. Sci.* **38**, 18 (1973).
- 16 B. An, S. Fukuyama, K. Yokogawa, and M. Yoshimura, *Phys. Rev. B* **68**, 115423 (2003).
- 17 Y. Li, B. An, S. Fukuyama, K. Yokogawa, and M. Yoshimura, *Mater. Charact.* **48**, 163 (2002).
- 18 R. D. Veit, R. G. Farber, N. S. Sitaraman, T. A. Arias, and S. J. Sibener, *J. Chem. Phys.* **152**, 214703 (2020).
- 19 R. D. Veit, N. A. Kautz, R. G. Farber, and S. J. Sibener, *Surf. Sci.* **688**, 63 (2019).
- 20 Y. Uehara, T. Fujita, M. Iwami, and S. Ushioda, *Surf. Sci.* **472**, 59 (2001).
- 21 I. Arfaoui, J. Cousty, and C. Guillot, *Surf. Sci.* **557**, 119 (2004).
- 22 I. Arfaoui, C. Guillot, J. Cousty, and C. Antoine, *J. Appl. Phys.* **91**, 9319 (2002).
- 23 M. Grundner and J. Halbritter, *J. Appl. Phys.* **51**, 397 (1980).
- 24 Y. Wang, X. Wei, Z. Tian, Y. Cao, R. Zhai, T. Ushikubo, K. Sato, and S. Zhuang, *Surf. Sci.* **372**, L285 (1997).
- 25 R. Franchy, T. U. Bartke, and P. Gassmann, *Surf. Sci.* **366**, 60 (1996).
- 26 C. Sürgers, M. Schöck, and H. V. Löhneysen, *Surf. Sci.* **471**, 209 (2001).
- 27 A. A. McMillan, J. D. Graham, S. A. Willson, R. G. Farber, C. J. Thompson, and S. J. Sibener, *Supercond. Sci. Technol.* **33**, 105012 (2020).
- 28 I. Estermann and O. Stern, *Z. Phys.* **61**, 95 (1930).
- 29 J. P. Toennies, *J. Phys.: Condens. Matter* **5**, A25 (1993).
- 30 E. Hulpke, *Helium Atom Scattering from Surfaces* (Springer-Verlag, Berlin, 1992).
- 31 *Atomic and Molecular Beam Methods*, edited by G. Scoles (Oxford University Press, New York, 1988), Vol. 1.
- 32 *Atomic and Molecular Beam Methods*, edited by G. Scoles (Oxford University Press, New York, 1992), Vol. 2.
- 33 B. Holst, G. Alexandrowicz, N. Avidor, G. Benedek, G. Bracco, W. E. Ernst, D. Fariás, A. P. Jardine, K. Lefmann, J. R. Manson, R. Marquardt, S. M. Artés, S. J. Sibener, J. W. Wells, A. Tamtögl, and W. Allison, *Phys. Chem. Chem. Phys.* **23**, 7653 (2021).
- 34 G. Benedek and J. P. Toennies, *Surf. Sci.* **299–300**, 587 (1994).
- 35 D. Fariás and K.-H. Rieder, *Rep. Prog. Phys.* **61**, 1575 (1998).
- 36 G. Benedek and J. P. Toennies, *Atomic Scale Dynamics at Surfaces* (Springer-Verlag, Berlin, 2018).
- 37 E. Hulpke, M. Hüppauff, D.-M. Smilgies, A. D. Kulkarni, and F. W. de Wette, *Phys. Rev. B* **45**, 1820 (1992).
- 38 P. H. Dederichs, H. R. Schober, and D. J. Sellmyer, *Phonon States of Elements. Electron States and Fermi Surfaces of Alloys* (Springer-Verlag, Berlin, Heidelberg, 1981).
- 39 Y. Nakagawa and A. D. B. Woods, *Phys. Rev. Lett.* **11**, 271 (1963).
- 40 R. I. Sharp, *J. Phys. C: Solid State Phys.* **2**, 421 (1969).
- 41 R. I. Sharp, *J. Phys. C: Solid State Phys.* **2**, 432 (1969).
- 42 P. Geerlings, F. De Proft, and W. Langenaeker, *Chem. Rev.* **103**, 1793 (2003).
- 43 B. Gans, P. A. Knipp, D. D. Koleske, and S. J. Sibener, *Surf. Sci.* **264**, 81 (1992).
- 44 D. D. Koleske and S. J. Sibener, *Rev. Sci. Instrum.* **63**, 3852 (1992).
- 45 B. R. King, H. C. Patel, D. A. Gulino, and B. J. Tatarchuk, *Thin Solid Films* **192**, 351 (1990).
- 46 A. Daccà, G. Gemme, L. Mattera, and R. Parodi, *Appl. Surf. Sci.* **126**, 219 (1998).
- 47 H. Oechsner, J. Giber, H. J. Füsler, and A. Darlinski, *Thin Solid Films* **124**, 199 (1985).
- 48 M. C. Payne, M. P. Teter, D. C. Allan, T. A. Arias, and J. D. Joannopoulos, *Rev. Mod. Phys.* **64**, 1045 (1992).
- 49 R. Sundararaman, K. Letchworth-Weaver, K. A. Schwarz, D. Gunceler, Y. Ozhaves, and T. A. Arias, *SoftwareX* **6**, 278 (2017).
- 50 J. P. Perdew, A. Ruzsinszky, G. I. Csonka, O. A. Vydrov, G. E. Scuseria, L. A. Constantin, X. Zhou, and K. Burke, *Phys. Rev. Lett.* **100**, 136406 (2008).
- 51 K. F. Garrity, J. W. Bennett, K. M. Rabe, and D. Vanderbilt, *Comput. Mater. Sci.* **81**, 446 (2014).
- 52 A. M. Brown, R. Sundararaman, P. Narang, W. A. Goddard III, and H. A. Atwater, *ACS Nano* **10**, 957 (2016).
- 53 N. Marzari and D. Vanderbilt, *Phys. Rev. B* **56**, 12847 (1997).
- 54 G. I. González-Pedrerros, J. A. Camargo-Martínez, and F. Mesa, *Sci. Rep.* **11**, 7646 (2021).
- 55 G. M. Eliashberg, *Sov. Phys. JETP* **11**, 696 (1960).
- 56 A. M. Brown, R. Sundararaman, P. Narang, W. A. Goddard III, and H. A. Atwater, *Phys. Rev. B* **94**, 075120 (2016).
- 57 P. B. Allen, *Phys. Rev. B* **6**, 2577 (1972).
- 58 F. Giustino, M. L. Cohen, and S. G. Louie, *Phys. Rev. B* **76**, 165108 (2007).
- 59 W. H. Butler, F. J. Pinski, and P. B. Allen, *Phys. Rev. B* **19**, 3708 (1979).
- 60 I. Y. Sklyadneva, G. Benedek, E. V. Chulkov, P. M. Echenique, R. Heid, K. P. Bohnen, and J. P. Toennies, *Phys. Rev. Lett.* **107**, 095502 (2011).
- 61 A. Tamtögl, P. Kraus, M. Mayrhofer-Reinhartshuber, D. Campi, M. Bernasconi, G. Benedek, and W. E. Ernst, *Phys. Rev. B* **87**, 035410 (2013).
- 62 G. Benedek, M. Bernasconi, K.-P. Bohnen, D. Campi, E. V. Chulkov, P. M. Echenique, R. Heid, I. Y. Sklyadneva, and J. P. Toennies, *Phys. Chem. Chem. Phys.* **16**, 7159 (2014).
- 63 J. R. Manson, G. Benedek, and S. Miret-Artés, *J. Phys. Chem. Lett.* **7**, 1016 (2016).
- 64 P. Hofmann, I. Y. Sklyadneva, E. D. L. Rienks, and E. V. Chulkov, *New J. Phys.* **11**, 125005 (2009).

⁶⁵V. Bortolani, A. Franchini, N. Garcia, F. Nizzoli, and G. Santoro, *Phys. Rev. B* **28**, 7358 (1983).

⁶⁶G. Benedek, M. Bernasconi, V. Chis, E. Chulkov, P. M. Echenique, B. Hellsing, and J. Peter Toennies, *J. Phys.: Condens. Matter* **22**, 084020 (2010).

⁶⁷J. Kröger, *Rep. Prog. Phys.* **69**, 899 (2006).

⁶⁸T. Miyake and H. Petek, *Appl. Surf. Sci.* **121–122**, 138 (1997).

⁶⁹J. F. Van Der Veen and J. W. M. Frenken, *Surf. Sci.* **178**, 382 (1986).

⁷⁰B. Pluis, A. W. D. van der Gon, J. W. M. Frenken, and J. F. van der Veen, *Phys. Rev. Lett.* **59**, 2678 (1987).

⁷¹J. P. Charlesworth, I. MacPhail, and P. E. Madsen, *J. Mater. Sci.* **5**, 580 (1970).

⁷²R. G. Farber, S. A. Willson, and S. J. Sibener, *J. Vac. Sci. Technol. A* **39**, 063212 (2021).